

Article

# Three-Dimensional Thermohaline Reconstruction Driven by Satellite Sea Surface Data Based on Sea Ice Seasonal Variation in the Arctic Ocean

**Xiangyu Wu** <sup>1,\*</sup>, **Jinlong Li** <sup>2</sup>, **Xidong Wang** <sup>2,3</sup>, **Zikang He** <sup>2</sup>, **Zhiqiang Chen** <sup>4</sup> , **Shihe Ren** <sup>1</sup> and **Xi Liang** <sup>1</sup> 

<sup>1</sup> National Marine Environmental Forecasting Center, Ministry of Natural Resources, Beijing 100081, China; rensh@nmefc.cn (S.R.); liangx@nmefc.cn (X.L.)

<sup>2</sup> Key Laboratory of Marine Hazards Forecasting, Ministry of Natural Resources, Hohai University, Nanjing 210098, China; 221611010009@hhu.edu.cn (J.L.); xidong\_wang@hhu.edu.cn (X.W.); hezikang@hhu.edu.cn (Z.H.)

<sup>3</sup> Southern Marine Science and Engineering Guangdong Laboratory (Zhuhai), Zhuhai 519000, China

<sup>4</sup> State Key Laboratory of Tropical Oceanography, South China Sea Institute of Oceanology, Chinese Academy of Sciences, Guangzhou 510070, China; zhiqiang\_chen@hhu.edu.cn

\* Correspondence: wxy@nmefc.cn

**Abstract:** This study investigates and evaluates methods for the three-dimensional thermohaline reconstruction of the Arctic Ocean using multi-source observational data. A multivariate statistical regression model based on sea ice seasonal variation is developed, driving by satellite data, and in situ data is used to validate the model output. The study indicates that the multivariate statistical regression model effectively captures the characteristics of the three-dimensional thermohaline structure of the Arctic Ocean. Areas with large reconstruction errors are primarily observed in the salinity values of ice-free regions and the temperature values of ice-covered regions. The statistical regression experiments reveal that salinity errors in ice-free regions are caused by inaccuracies in the satellite salinity data, while temperature errors in ice-covered areas mainly result from the inadequate representation of the under-ice temperature structure of the reanalysis data. The continuous and stable thermohaline data produced using near real-time satellite data as input provide an important foundation for studying Arctic marine environmental characteristics and assessing climate change.

**Keywords:** sea ice seasonal variation; statistical regression model; idealized experiment; three-dimensional thermohaline structure; reconstruction



**Citation:** Wu, X.; Li, J.; Wang, X.; He, Z.; Chen, Z.; Ren, S.; Liang, X. Three-Dimensional Thermohaline Reconstruction Driven by Satellite Sea Surface Data Based on Sea Ice Seasonal Variation in the Arctic Ocean. *Remote Sens.* **2024**, *16*, 4072. <https://doi.org/10.3390/rs16214072>

Academic Editor: Chung-Ru Ho

Received: 11 September 2024

Revised: 12 October 2024

Accepted: 14 October 2024

Published: 31 October 2024



**Copyright:** © 2024 by the authors. Licensee MDPI, Basel, Switzerland. This article is an open access article distributed under the terms and conditions of the Creative Commons Attribution (CC BY) license (<https://creativecommons.org/licenses/by/4.0/>).

## 1. Introduction

Arctic environmental characteristics serve both as sensitive indicators of climate variability and change [1], and as active factors influencing these processes [2–4]. Against the backdrop of global warming, the Arctic amplification effect exacerbates the reduction in sea ice cover [5], thereby greatly impacting the global environment [6,7]. The coupling of sea ice, seawater and atmosphere is a primary feature of polar environmental changes. Meanwhile, the continuous increase in ice-free ocean areas and the widening of seasonal sea ice marginal zones affect the interactions among atmosphere, sea ice, and ocean, subsequently influencing the upper ocean structure, water masses, and sea ice evolution. In addition, the harsh natural and geographical conditions of the Arctic result in a spatiotemporal uneven distribution of in situ observational data, which is insufficient to describe the internal structure and change patterns of the Arctic Ocean. Therefore, with the advancement of satellite remote sensing observation technology, using high spatiotemporal resolution ocean satellite remote sensing data and constructing three-dimensional thermohaline structure statistical regression models to establish the three-dimensional thermohaline structure of Arctic Ocean is of great significance for studying Arctic oceanic phenomena and ice–sea–air interactions.

The Arctic Ocean possesses a complex thermohaline circulation. In the Nordic Area, the main currents consist of the northward-flowing North Atlantic Current entering the Arctic Ocean and the southward-flowing East Greenland Current exiting it. The North Atlantic Current flows into the Norwegian Sea, where it joins the Norwegian Atlantic Current (NAC). The NAC, along with the Norwegian Coastal Current, flows northward to the northern edge of Norway, where it splits into two branches. One branch flows eastward into the Barents Sea and eventually into the Arctic Ocean, while the other flows westward towards Svalbard (Spitsbergen), where it splits again. One part, known as the West Spitsbergen Current (WSC), flows through the Fram Strait into the Arctic Ocean, and the other turns southward, joining the East Greenland Current (EGC). The surface circulation in the Eurasian Basin and the marginal seas of the Arctic Ocean is generally cyclonic, while in the Canadian Basin, there is an anticyclonic Beaufort Gyre. Additionally, the Arctic Ocean features the Transpolar Drift, a major surface current that flows from the Siberian coast across the central Arctic Ocean toward the Fram Strait, transporting sea ice and water masses from the Russian Arctic to the North Atlantic.

The three-dimensional thermohaline structure is a fundamental environmental element of the ocean and an essential condition for studying ocean circulation and water masses. The current methods for reconstructing the three-dimensional thermohaline structure primarily include assimilation and fusion of different data sources using numerical models with physical equations based on simplified dynamical models [8,9], and establishing relationships between sea surface and subsurface ocean elements using statistical methods [10–12]. Additionally, artificial intelligence has provided new approaches for inverting three-dimensional ocean fields [13,14].

At first, statistical methods mostly decomposed the temperature observation profile cargo volume height into EOF to find the regression relationship between the amplitude corresponding to certain modes and SST or SSH, and to achieve the goal of reconstructing the temperature field [15–17]. Due to the late emergence of salinity observations, this early statistical method only inverted the temperature field. Fox [10] and Guinehut [18] used regression analysis to statistically analyze the correlation between sea surface temperature, sea surface height, and temperature profiles based on historical observations of temperature and salinity profiles. Then, they used satellite remote sensing of sea surface temperature and satellite observation of sea surface height information to reconstruct a high-resolution spatiotemporal three-dimensional thermohaline field of the ocean (MODAS). This method has been widely applied and tested in mid to low latitude waters, such as the Northwest Pacific, North Indian Ocean, and South China Sea [19–21], but has not yet been validated in polar regions. Helber et al. [22] divided the ocean into three layers and improved the reconstruction of the three-dimensional thermohaline field using variational methods in the thermocline (ISOP). Compared with statistical regression methods, variational methods have more constraint terms and significantly improve the reconstructed thermocline field [23]. However, the effectiveness of this stratification method in the Arctic sea area with its complex dynamic processes still needs to be verified.

Hurlburt [24] used a simple two-layer model based on the ocean dynamic model to calculate the corresponding subsurface structure through surface pressure. Haines [25] used a four layer quasi geostrophic (QG) model to assimilate altimeter data and assumed the conservation of subsurface potential eddies during the assimilation process. Lapeyre and Klein [8] proposed the eSQG method that couples surface buoyancy with subsurface potential vortices. The eSQG method performs well in the upper 500 m layer [26] and has been successfully applied in some studies [27–30]. In addition, Wang et al. [9] proposed the isQG method for inverting the density and velocity fields of the subsurface in three square regions of the Gulf Stream. The applicability of the isQG method in multiple strong current regions, such as the Gulf Stream, Kuroshio Current, and Agulhas system, has been verified through numerical simulation data [9,31,32]. However, the dynamic mapping method is more suitable for regional scales and relies too much on input parameters to retrieve large-scale subsurface information.

Han et al. [13] proposed a convolutional neural network method for predicting the subsurface sea temperature based on the sea surface temperature, sea surface height, and sea surface salinity data. They established CNN models for different months to predict and reconstruct the subsurface sea temperature in the Pacific Ocean and compared them with Argo field data to verify accuracy. The results showed that the established model could accurately estimate the subsurface sea temperature in the Pacific Ocean. Su et al. [33] proposed a method based on a CNN model that combines satellite remote sensing and profiling buoy observation data to invert the high-resolution seawater temperature field of the global ocean from 0 to 1000 m. Based on the proposed method, the spatial resolution of the seawater temperature field was increased from  $1^\circ$  to  $0.25^\circ$ . Meng et al. [34] proposed a method for predicting the subsurface temperature field based on a combination of generative adversarial networks (GANs) and numerical models. The method first learns the simplified physical relationship between sea surface temperature and subsurface seawater temperature in the numerical model based on the GAN model, and then calibrates the network model parameters with Argo data to obtain better predictions, effectively utilizing the advantages of numerical models and neural networks. Yang et al. [35] provided a more detailed introduction to the research progress of using AI methods to invert three-dimensional temperature and salinity fields. Classic deep learning techniques such as CNN have been widely applied in the intelligent detection of three-dimensional temperature and salinity fields, but the internal operating mechanism of intelligent models is invisible and cannot check the logic of output results or the code of the system.

In summary, we have chosen a statistical method that has undergone extensive testing, is easy to operate, and possesses a logical understanding of the output. Based on the seasonal changes and temperature salinity characteristics of Arctic sea ice, we introduce sea ice density as a control variable and reconstruct three-dimensional temperature salinity based on SST, SLA, and SSS.

This study, referencing the MODAS method and comprehensively considering Arctic sea ice seasonal variations, based on reanalysis data, establishes regression models between sea surface information and subsurface information for the Arctic region (Figure 1,  $60^\circ\text{N}$ – $90^\circ\text{N}$ ,  $180^\circ\text{W}$ – $180^\circ\text{E}$ ). The inversion results are evaluated to ultimately obtain a three-dimensional thermohaline structure of the Arctic seas with a daily spatial resolution of  $12.5\text{ km} \times 12.5\text{ km}$ .

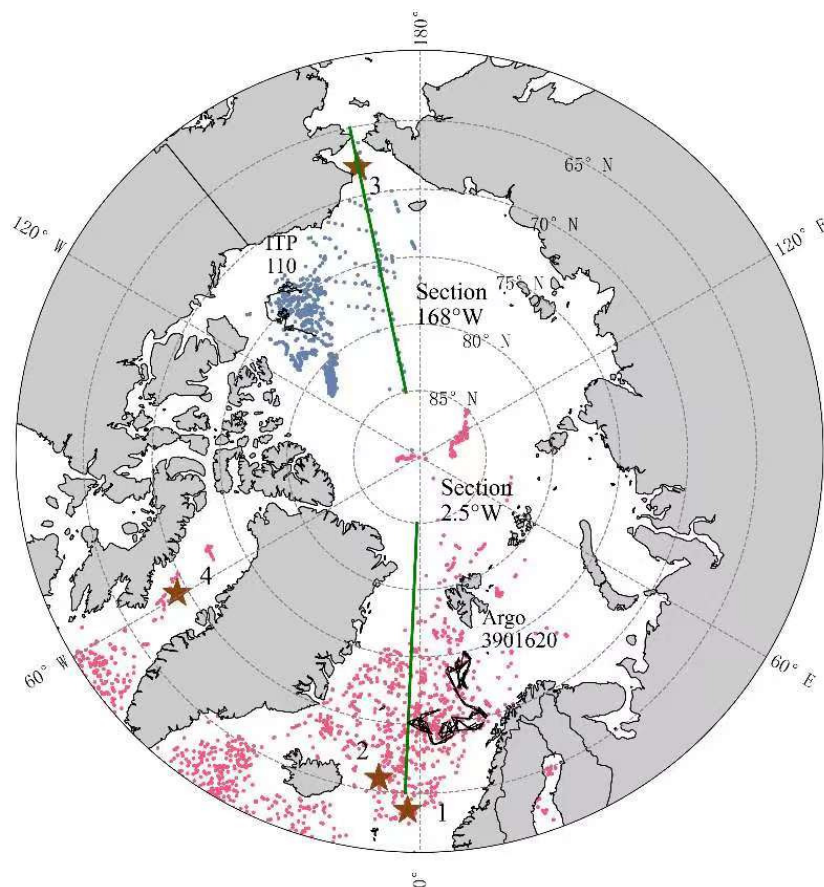


**Figure 1.** Study area ( $60^{\circ}\text{N}$ – $90^{\circ}\text{N}$ ). The two green lines are the positions of the cross-sections analysis; details are in Figure 9. The two black lines are the traces of Argo and ITP that we chose in a period; details are in Figure 11 and Figure 12. The four star points are the positions we chose to show the comparation of three kinds of data; details are in Figure 14. The pink and blue dots stand for the positions that we chose from the in situ dataset.

## 2. Materials and Methods

### 2.1. Data

Satellite Sea Surface Temperature (SST), Satellite Sea Ice Concentration (SIC)

The satellite SST and SIC data used in this study are obtained from OSTIA [36–38], which, produced by the UK Met Office, provides daily global sea surface temperature and sea ice concentration products at a  $1/20^{\circ}$  resolution.

Satellite Sea Level Anomaly (SLA)

The SLA data used in this study are obtained from Aviso's [39] multi-source merged sea level anomaly product for the Arctic. This data product is derived from three satellites: SARAL/AltiKa, Cryosat-2, and Copernicus Sentinel-3A, with the final multi-mission gridded product generated through optimal interpolation.

Satellite Sea Surface Salinity (SSS)

The SSS data used in this study are sourced from the Barcelona Expert Center soil moisture and ocean salinity (BEC-SMOS) product, which has been operational since January 1, 2011. This product is specifically designed for the Arctic and sub-Arctic seas ( $50^{\circ}\text{N}$ – $90^{\circ}\text{N}$ ) and provides 9-day SMOS-SSS data at a 25 km resolution [40]. It applies a time-dependent bias correction to mitigate the seasonal biases previously present in SSS data.

### 2.1.1. Reanalysis Data

The reanalysis data were taken from the TOPAZ4b version [41,42], hereafter referred to as the TOPAZ reanalysis data, which include physical quantities such as temperature, salinity, sea ice concentration, and sea ice thickness. The TOPAZ reanalysis data have a horizontal resolution of  $12.5 \times 12.5$  km and a daily temporal resolution, covering the spatial range of  $50^{\circ}\text{N}$ – $90^{\circ}\text{N}$ ,  $180^{\circ}\text{W}$ – $179.88^{\circ}\text{E}$ , and spanning the time range of 1991–2023. TOPAZ [43] is a coupled sea ice data assimilation system for the North Atlantic and Arctic. This system is based on the Hybrid Coordinate Ocean Model (HYCOM).

### 2.1.2. In Situ Observation

**Chinese Arctic research expedition:** China has accumulated over two decades of experience in Arctic marine environmental scientific surveys. Using the Xuelong and Xuelong 2 icebreakers, Chinese teams have conducted comprehensive surveys at the North Pole, around the Arctic Ocean. They have also carried out scientific investigations in areas such as the Chukchi, East Siberian and Beaufort Seas, amassing a wealth of first-hand observational data.

**Array for Real-time Geostrophic Oceanography (Argo):** In the late 1990s, scientists from the US, Japan, and other countries initiated the international Argo program [44]. The program envisioned establishing a vast global ocean observation network to obtain near real-time, wide-ranging, and high-resolution global ocean data. Argo is an international program that collects information from within the ocean using a fleet of robotic instruments that drift with ocean currents and move up and down between the surface and at mid-water level. Each instrument (float) spends almost its entire life below the surface. The global Argo ocean observation network has now been fully established, with the cumulative number of temperature and salinity profiles collected exceeding 2 million as of 2018.

**Ice-Tethered Profiler (ITP):** To address the scarcity of under-ice thermohaline observations compared to the open ocean, the Woods Hole Oceanographic Institution deployed a new instrument called the “Ice-Tethered Profiler” (ITP) [45] in the Arctic waters. This is analogous to the international Argo float program, which employs autonomous profiling floats to return real-time seawater property data from the ice-covered Arctic Ocean at high vertical resolution for periods of up to three years. ITP can help us better understand the coupled atmosphere–ice ocean system in the Arctic.

### 2.1.3. Climatology Data

The thermohaline climatology data used in this study are derived from the Polar Science Center Hydrographic Climatology (PHC3.0) dataset [46]. This dataset integrates the World Ocean Atlas (WOA) and Arctic Ocean Atlas (AOA). The spatial coverage of the dataset extends from  $89.5^{\circ}\text{S}$  to  $89.5^{\circ}\text{N}$  and  $179.5^{\circ}\text{W}$  to  $179.5^{\circ}\text{E}$ . The monthly climatology is used with a horizontal resolution of  $1^{\circ} \times 1^{\circ}$  and vertical depths ranging from 0 to 1500 m to validate and evaluate the inversion results.

We have summarized the roles of different data in Table 1.

**Table 1.** Data Description.

Type	Project	Description	Purpose
SST	OSTIA	$1/20^{\circ}$ , daily	Input for reconstruction
SLA	Avsio	$1/4^{\circ}$ , 3-days mean, 3-d	Input for reconstruction
SSS	SMOS	$25 \text{ km} \times 25 \text{ km}$ , 9-days mean, daily	Input for reconstruction
SIC	OSTIA	$1/20^{\circ}$ , daily	Input for reconstruction
Reanalysis	TOPAZ	$12.5 \text{ km} \times 12.5 \text{ km}$ , daily	Calculate and compare Input for reconstruction
Climatology	PHC3.0	$1^{\circ} \times 1^{\circ}$ , monthly	Compare
In situ obs.	Argo etc.	Scatter data	Compare

## 2.2. Methods

### 2.2.1. Reconstruction Method

In general, this study employs a traditional statistical mapping approach, considering the influence of Arctic sea ice on the three-dimensional temperature and salinity structure. Using sea ice concentration as a criterion, the study area is dynamically divided into ice-covered and ice-free regions. Based on the characteristics of water masses in different areas, the statistical regression models are established for the vertical distribution characteristics of both temperature and salinity using TOPAZ reanalysis data, as illustrated in Figure 2.

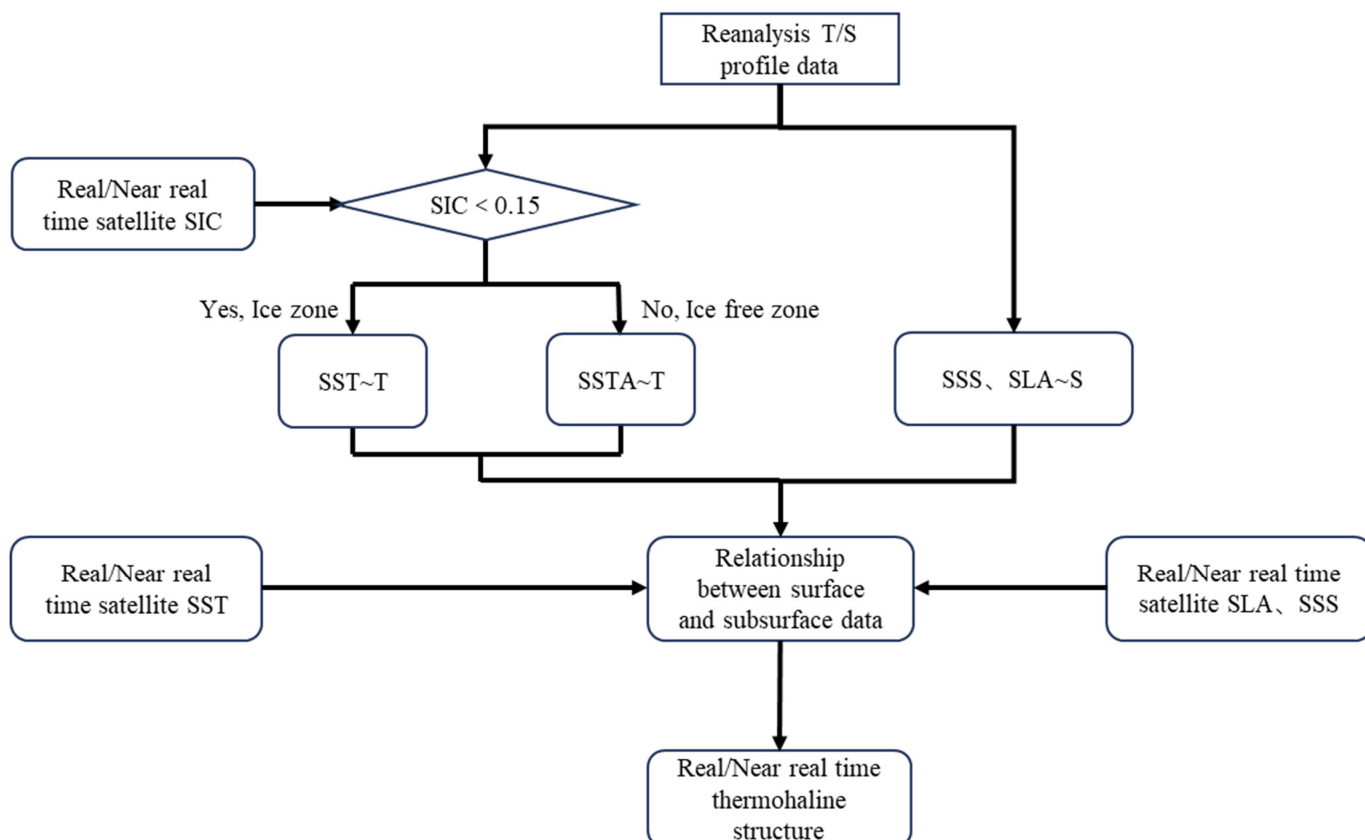


**Figure 2.** Reconstruction process of the three-dimensional thermohaline structure.

For the construction of the statistical regression model for temperature profiles, this study defined ice-covered and ice-free areas based on the seasonal sea ice variation characteristics in the Arctic and temperature features under different sea conditions. Sea Ice Concentration (SIC) is used as the criterion, following the convention in sea ice research. We define regions with sea ice concentrations below 15% as ice-free areas, and those with concentrations above 15% as ice-covered areas [47–52]. On this basis, the mapping relationships between sea surface and subsurface temperatures are created for both ice-covered and ice-free regions. The regression equation for an ice-covered region between sea surface temperature and temperature profile is given by Equation (1), and that for ice-free region by Equation (2):

$$T_{i,k}(SST) = B_{i,k} + a_{i,k}^{T_1} * SST \quad (1)$$

$$T_{i,k}(SST) = \bar{T}_{i,k} + a_{i,k}^{T_1}(SST - \bar{T}_{i,1}) \quad (2)$$

where  $\bar{T}_{i,k}$  is the average temperature at the  $k$ -th layer of analysis point  $i$ , calculated by Equation (2);  $a_{i,k}^{T_1}$  is the regression coefficient at the  $k$ -th layer of analysis point  $i$ , calculated by Equation (3);  $SST$  is the satellite-derived sea surface temperature;  $\bar{T}_{i,1}$  is the average sea

surface temperature at analysis point  $i$ ; and  $B_{i,k}$  is the correction coefficient at the  $k$ -th layer of analysis point  $i$ :

$$a = (XX')^{-1}X'Y \quad (3)$$

where  $X$  is the augmented matrix of TOPAZ reanalysis sea surface temperature data; and  $Y$  is the temperature at specific layers from the TOPAZ reanalysis data.

Analysis of the results shows that the TOPAZ reanalysis data processing for sea surface temperature in ice-covered areas differs from the satellite data, which affects the calculation of the regression coefficients. Therefore, when calculating the temperature regression coefficients and correction coefficients for ice-covered areas, a correction relative to  $-1.8^{\circ}\text{C}$  [51] is applied to the reanalysis surface data under ice to match the satellite data used as the true input.

Considering the complex under-ice thermohaline relationships in the Arctic regions—particularly in the central Arctic areas represented by the Beaufort Sea, where salinity changes are the primary cause of SLA variations [53,54]—the traditional thermohaline relationship is not used when inverting salinity profiles. Instead, the three-dimensional salinity structure of the Arctic region is reconstructed by calculating sea level anomalies and regression coefficients between sea surface salinity and subsurface salinity [55]. Since satellite data products lack SSS data below ice surfaces, the statistical regression method used in this study omits the SSS term in ice-covered areas.

The regression equation for the relationship between sea level anomaly and salinity profile is given by Equation (4):

$$S_{i,k}(SLA, SSS) = \bar{S}_{i,k} + a_{i,k}^{S_1}(SLA - \overline{SLA}_i) + a_{i,k}^{S_2}(SSS - \overline{SSS}_i) \quad (4)$$

where  $a_{i,k}^{S_1}$  and  $a_{i,k}^{S_2}$  are calculated using the same approach as in Equation (3);  $\overline{SLA}_i$  is the average sea level anomaly at analysis point  $i$ ; and  $\overline{SSS}_i$  is the average sea surface salinity at analysis point  $i$ .

## 2.2.2. Validation Method

Root Mean Square Error ( $RMSE$ ) is often used to measure the deviation between observed values and true values. Due to its high sensitivity to outliers, it is widely employed in atmospheric and oceanic fields for verification. In this study,  $RMSE$  is adopted to evaluate the error between the inverted results and observations:

$$RMSE_T = \sqrt{\frac{1}{N} \sum_{i=1}^N (T_R - T_o)^2} \quad (5)$$

$$RMSE_S = \sqrt{\frac{1}{N} \sum_{i=1}^N (S_R - S_o)^2} \quad (6)$$

where  $T_R$  and  $S_R$  are the inverted and reconstructed temperature and salinity results;  $T_o$  and  $S_o$  are the observed values; and  $N$  is the number of observations.

## 2.2.3. Others

Ocean Heat Content ( $OHC$ ) refers to the total amount of heat stored in the ocean. It is an important component of the climate system, and can directly reflect the characteristics of global and regional climate change, calculated by Equation (7):

$$OHC(t, x, y) = \int_{z_1}^{z_2} \rho_0 C_p T(t, x, y, z) dz \quad (7)$$

where  $\rho_0$  is the density of seawater;  $C_p$  is the specific heat capacity of seawater;  $T$  is the seawater temperature;  $z_1$  is the lower boundary depth of integration; and  $z_2$  is the upper boundary depth of integration.

Specific Volume Anomaly ( $h$ ) refers to the difference in the specific volume of seawater relative to a reference state (0 °C, 35 psu). It is calculated from changes in specific volume to determine sea surface height variations. This anomaly reflects changes in seawater volume due to density variations, and is calculated using Equation (8):

$$h = \int_0^H \frac{[\nu(T, S, p) - \nu(0, 35, p)]}{\nu(0, 35, p)} dz \quad (8)$$

where  $\nu$  is the specific volume of seawater;  $T$  is the temperature of seawater;  $S$  is the seawater salinity;  $p$  is the seawater pressure; and  $H$  is the integration depth.

### 3. Results

#### 3.1. Ideal Experiment

Although the three-dimensional thermohaline reconstruction method based on statistical mapping has been widely applied in mid-low latitudes oceans [56], experiments using this method have yet to be conducted in the Arctic region. The seasonal variations of Arctic sea ice significantly influence the underwater thermohaline structure in the Arctic seas. Therefore, in this study, we design an ideal experiment driven by reanalysis data to verify the reliability of the established statistical regression model based on seasonal sea ice variations in the Arctic region. First, TOPAZ surface data for the period of 2018–2020 are used as input to obtain inversion results with a spatial range of 60°N–90°N, 180°W–180°E, a spatial resolution of 12.5 km × 12.5 km, and a temporal resolution of daily data. The results from this ideal experiment are then averaged by month and interpolated to create a monthly climatology with a spatial range of 60°N–90°N, 180°W–180°E, and spatial resolution of 1° × 1°. The feasibility of the statistical regression model based on Arctic sea ice seasonal variation characteristics is then verified by comparing these results with the PHC climatology.

Figure 3 presents calculations of ocean heat content from both the ideal experiment and PHC climatology, focusing on March and September for characteristic analysis. The ideal experiment generally reflects the changing trends of shallow ocean heat content in the Arctic. Spatially, it is higher on the Atlantic side, decreasing as the North Atlantic warm current flows into the Arctic Ocean, while temporally it is lower in March than September, primarily due to seasonal sea ice variations.

Next, to further evaluate the feasibility of the statistical regression model based on seasonal sea ice variations and the validity of the produced data, 3109 observational data points from Argo, ITP, and Chinese Arctic scientific expeditions performed between 2018 and 2020 are randomly selected to create a comparative benchmark, and the distribution of these data points is shown in Figure 1. Next, both the ideal experiment inversion results and PHC climatology are interpolated to the location of each observation point, then the RMSE between the ideal experiment numerical results and PHC climatology were calculated. To match their temporal resolutions, the ideal experiment results are also processed into the monthly climatology. The results of this experiment are shown in Figure 4.

Figure 4 clearly demonstrates that the RMSE of the ideal experiment is lower than that of the PHC climatology at all depths. Moreover, the RMSE of the temperature inversion results is consistently below 1.0, while that of the salinity inversion results remains under 0.6. This indicates the rationality and effectiveness of the statistical regression model based on seasonal sea ice variations established in this study.

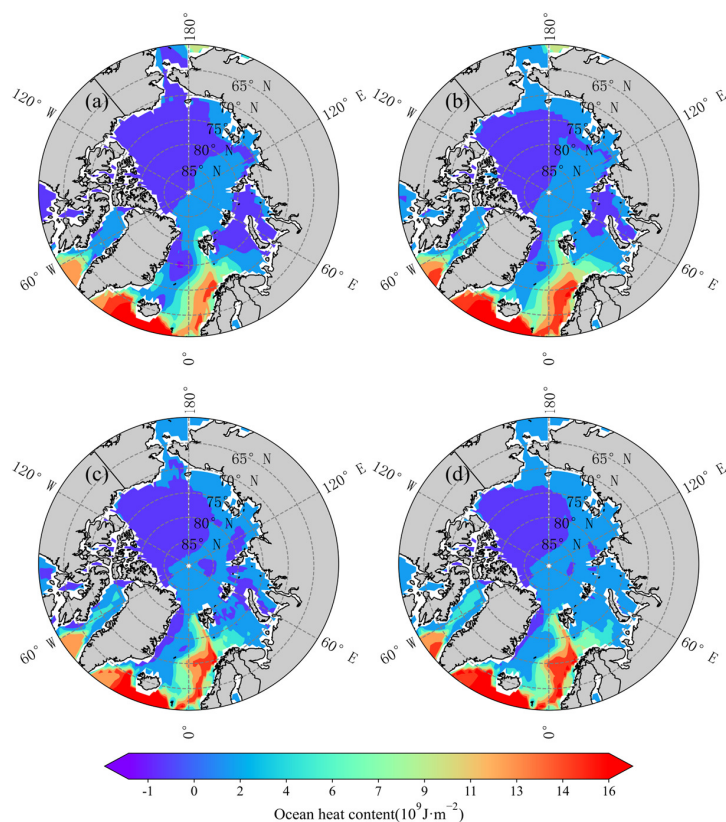


**Figure 3.** Comparison of ocean heat content between the ideal experiment and PHC climatology. Where (a,b) show the ocean heat contents above 700 m for March and September, respectively, from the ideal experiment; and (c,d) show those for the same months from the PHC climatology.

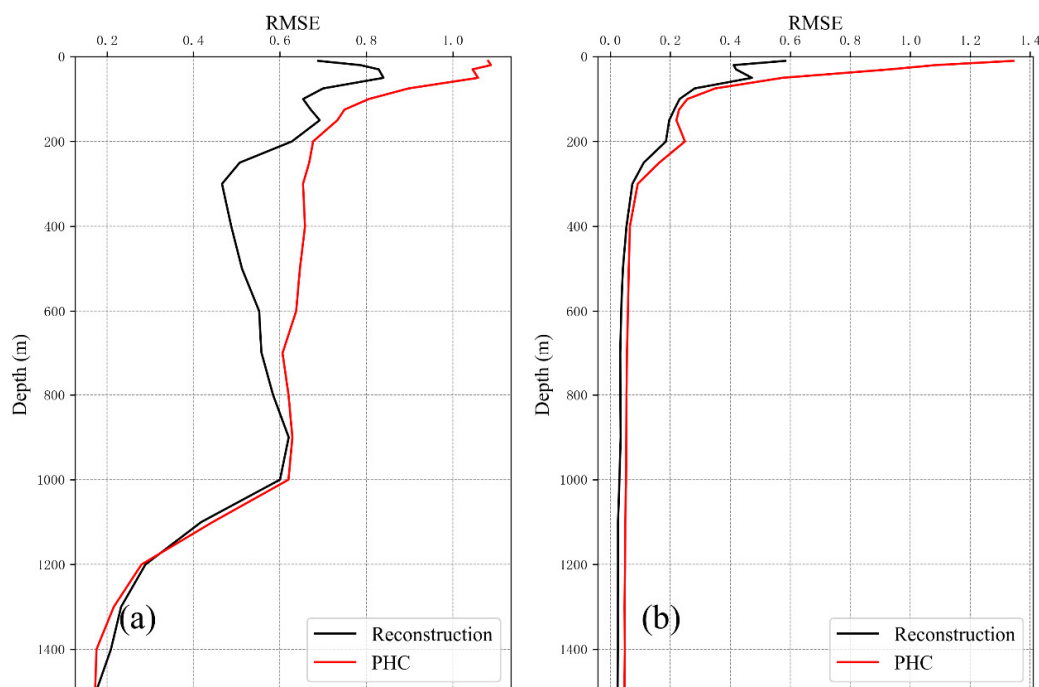


**Figure 4.** RMSE of ideal experiment and PHC climatology based on field observations. Where (a) shows the temperature RMSE, and (b) shows the salinity RMSE.

### 3.2. Satellite Data Driven

Subsequently, the SST and SIC, SLA data, and SSS for the period of 2018–2020 are used as inputs to calculate the three-dimensional thermohaline structure data results for

this time period. Considering the significant seasonal variations in Arctic sea ice, with the maximum ice extent typically occurring in March and the minimum in September, we selected 15 March and 15 September 2020 as the representative data. We directly compared the calculated satellite-driven results for the typical two days with the corresponding TOPAZ reanalysis data, as shown in Figures 5–8.

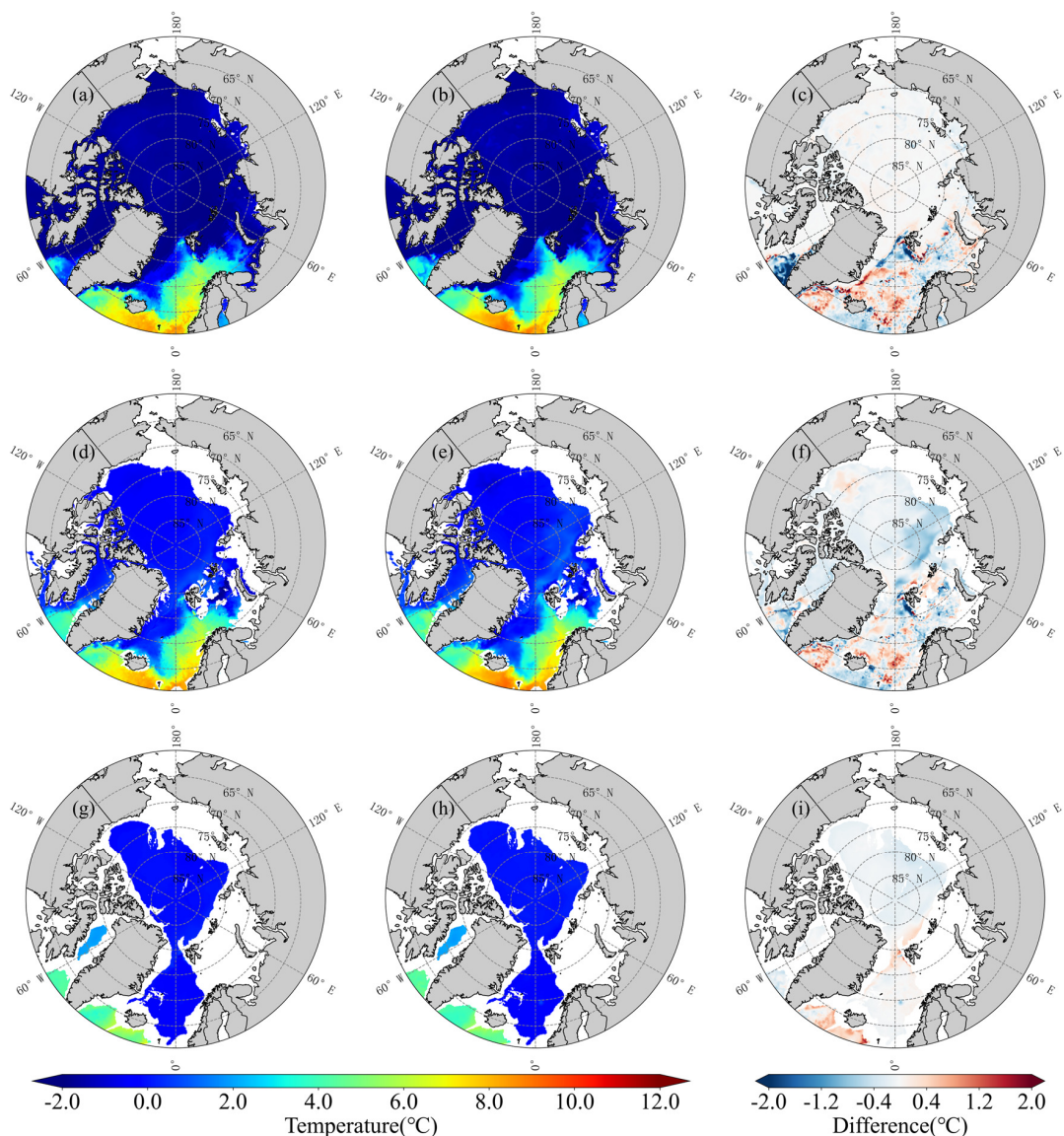


**Figure 5.** Comparison of reconstructed temperature and TOPAZ reanalysis on 15 March 2020. Where (a–c), respectively, show the reconstructed temperature field, TOPAZ temperature field, and the difference between the reconstructed and TOPAZ temperature fields at 10 m; (d–f) show those at 200 m; and (g–i) show those at 1200 m.

From Figure 5, it can be seen that the reconstructed temperature fields for winter at various depths and the reanalysis temperature fields both effectively reflect the spatial variation trends of temperature in the Arctic Ocean. However, there are differences between the reconstructed and reanalysis temperature. Specifically, the reconstructed temperature at 10 m shows a maximum difference of about 0.5 °C compared to the reanalysis temperature in the Nordic seas, while the difference is negligible in the central Arctic Ocean. This is because the central Arctic Ocean is covered by sea ice, which stabilizes the surface water temperature close to the freezing point. In the ice-free zone, a certain temperature deviation is reasonable due to the inherent errors in satellite SST and reanalysis data. Additionally,

the reconstructed temperature at the entrance of Baffin Bay shows a lower temperature, up to  $1.5^{\circ}\text{C}$  or so, which is due to the mismatch between the satellite SIC and reanalysis SIC. The significant difference in temperatures, particularly SST, between the ice zone and ice-free zone leads to larger errors in the reconstructed field compared to the reanalysis field. At 200 m depth, the error in the ice zone increases compared to 10 m, while the error in the ice-free zone decreases, but the overall temperature error in the Arctic Ocean tends to stabilize. At 1200 m depth, the temperature error across the Arctic Ocean is even smaller.

Figure 6, similar to Figure 5, shows that both the reconstructed and reanalysis salinity fields effectively reflect the spatial variation trends of salinity in the Arctic Ocean. The differences between them are greatest at 10 m, with salinity differences reaching up to 1 psu in coastal areas, and overall, salinity tends to be higher in the ice zone and lower in the ice-free zone. The salinity differences stabilize at 200 m and can be ignored at 1200 m.

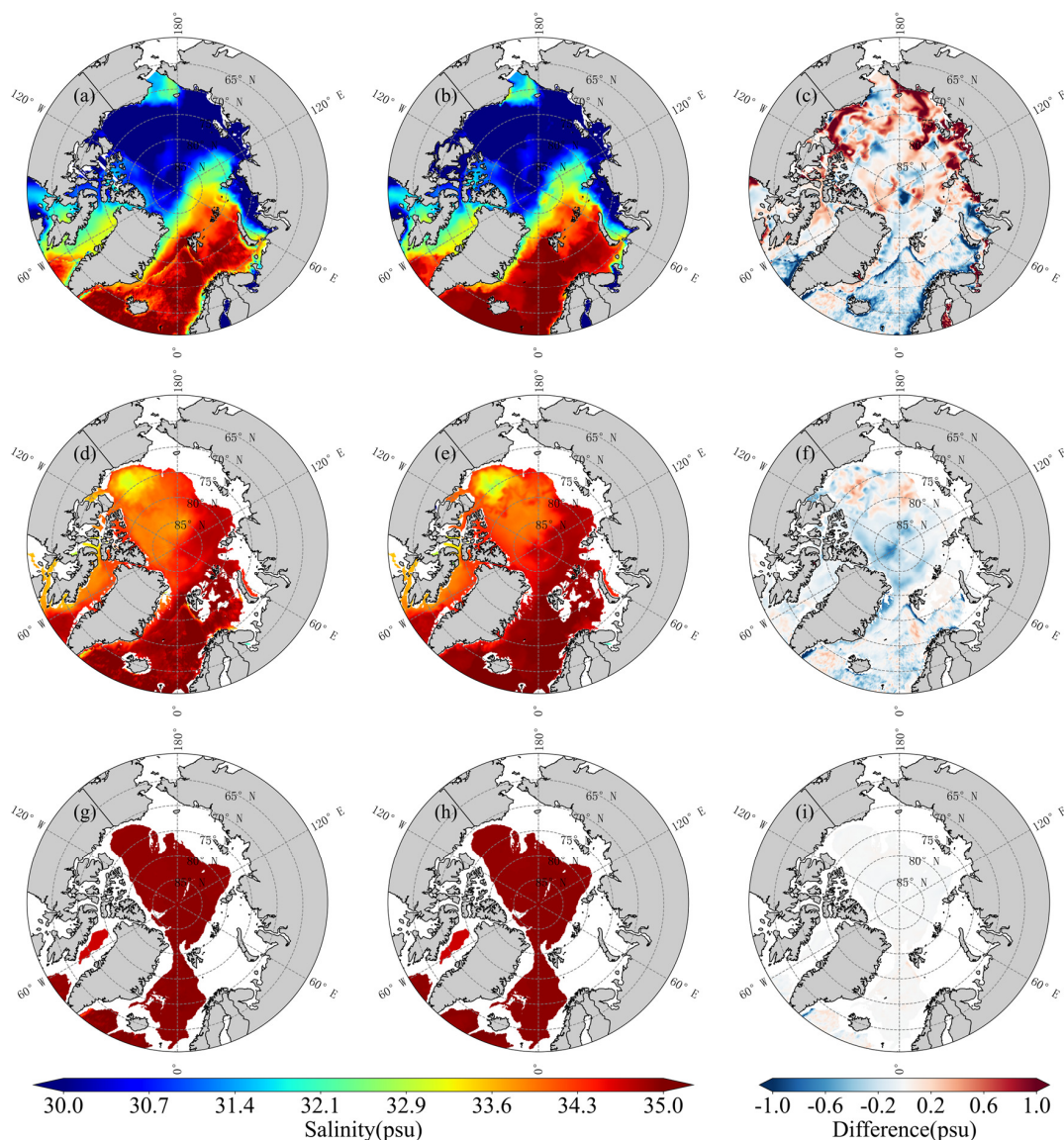


**Figure 6.** Comparison of reconstructed salinity field and TOPAZ reanalysis on 15 March 2020. Where (a–c), respectively, show the reconstructed salinity field, TOPAZ salinity field, and the difference between the reconstructed and TOPAZ salinity fields at 10 m; (d–f) show those at 200 m; and (g–i) show those at 1200 m.

Figure 7 shows that the overall trends of the reconstructed temperature fields and reanalysis temperature fields are consistent across all layers. However, there are significant

differences between the reconstructed and reanalysis temperature fields in the shallow layers. Specifically, at 10 m, lower temperatures are observed in the reconstructed temperature field in Baffin Bay and Hudson Bay compared to the reanalysis temperature field, with differences reaching about  $1.5^{\circ}\text{C}$ . This discrepancy is greatly reduced at 200 m, and almost disappears at 1200 m. Additionally, at 10 m, the reconstructed temperature field under the ice is about  $1^{\circ}\text{C}$  higher than the reanalysis temperature field. This is attributed to the temperature statistical regression model being driven by satellite SST data. When the satellite SST differs from the reanalysis surface data, the shallow layer results tend to align more closely with the satellite observations.

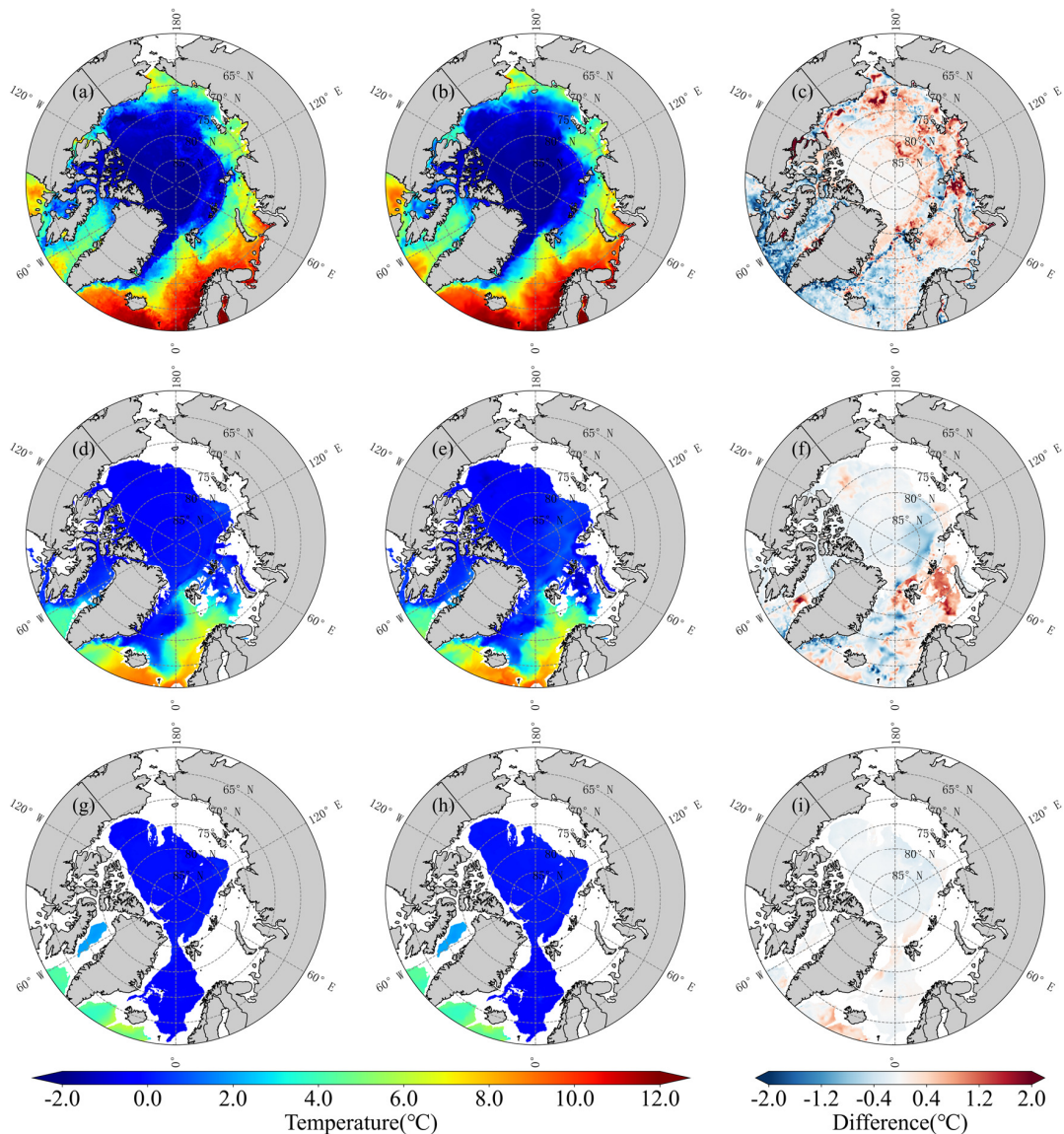


**Figure 7.** Comparison of reconstructed temperature and TOPAZ reanalysis on 15 September 2020. Where (a–c), respectively, show the reconstructed temperature field, TOPAZ temperature field, and the difference between the reconstructed and TOPAZ temperature fields at 10 m; (d–f) show those at 200 m; and (g–i) show those at 1200 m.

Consistent trends are observed between the reconstructed and reanalysis salinity fields across all layers. However, differences of about 1 psu are found between those at 10 m, decreasing as the depth increases. This is primarily attributed to the significant influence of sea ice melting on shallow layer salinity.

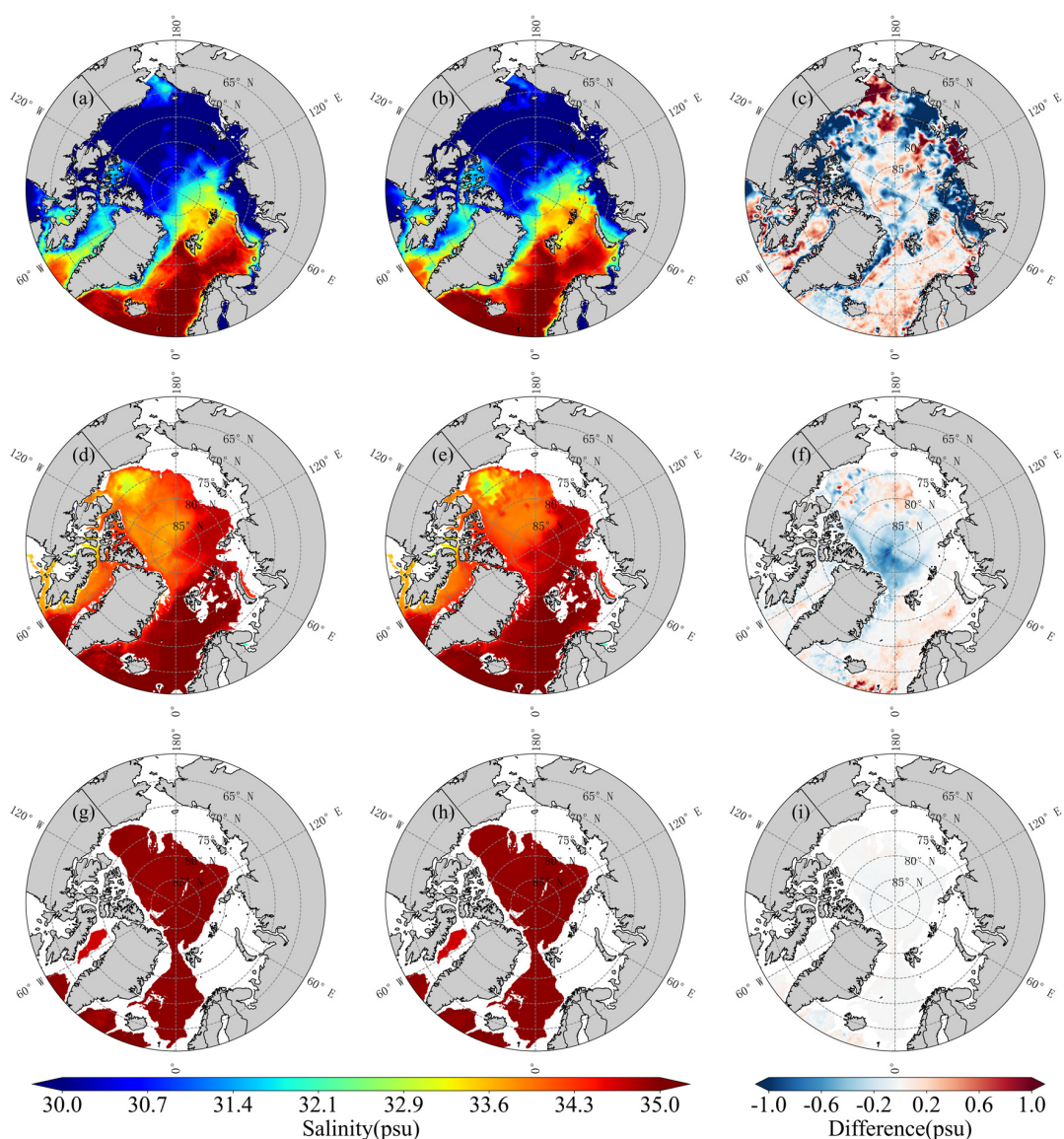


**Figure 8.** Comparison of reconstructed salinity field and TOPAZ reanalysis on 15 September 2020. Where (a–c), respectively, show the reconstructed salinity field, TOPAZ salinity field, and the difference between the reconstructed and TOPAZ salinity fields at 10 m; (d–f) show those at 200 m; and (g–i) show those at 1200 m.

Overall, the satellite-driven reconstruction results effectively reflect the spatial and seasonal variation trends of the three-dimensional temperature and salinity fields in the Arctic Ocean. Compared to the reanalysis data, the differences in the satellite-driven reconstruction results are mainly observed in the shallow layers, with smaller temperature differences in the ice zone and larger temperature differences in the ice-free zone. Additionally, salinity differences are more significant in coastal areas.

During the inversion process, due to the presence of Arctic sea ice, the Arctic region is divided into ice-covered and ice-free areas based on sea ice concentration. To verify the reliability of the results, two typical cross-sections are selected for evaluation, as shown in Figure 1, and the results are presented in Figure 9.

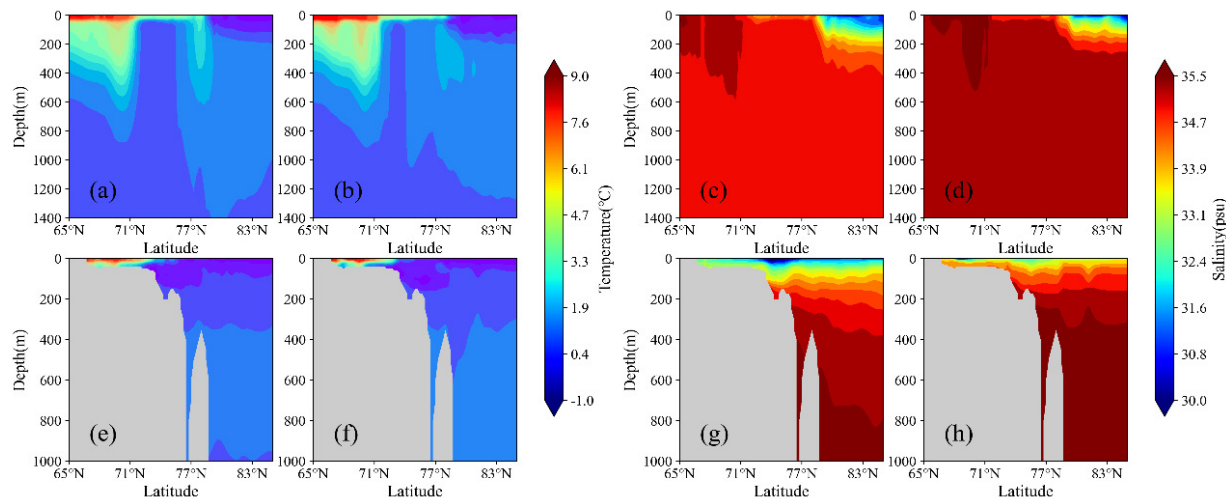


**Figure 9.** Thermohaline cross-sections of reconstructed data and reanalysis data on 15 September 2020. Where (a,b), respectively, show the reconstructed and reanalysis temperature results for the  $2.5^{\circ}\text{W}$  cross-section; (c,d) show those for the  $2.5^{\circ}\text{W}$  cross-section; (e,f) show those for the  $168^{\circ}\text{W}$  cross-section; and (g,h) show those for the  $168^{\circ}\text{W}$  cross-section.

The results indicate that the thermohaline variations in both cross-sections are well represented. For the  $2.5^{\circ}\text{W}$  one, the low-latitude region exhibits high temperature and high salinity characteristics, due to the influence of the North Atlantic. As the latitude increases, the temperature gradually decreases, and the shallow layer salinity increases with depth due to the influence of sea ice. For the  $168^{\circ}\text{W}$  cross-section, the reconstructed results show greater consistency with the reanalysis data. This also demonstrates the feasibility and effectiveness of the statistical regression method based on seasonal sea ice variations.

The uneven spatiotemporal distribution of observational data in the Arctic region poses challenges for model assimilation, in turn affecting the reanalysis data results. To further verify the results of the statistical regression model driven by satellite remote sensing data, the Argo and ITP field observation data shown in Figure 1 are selected for validation. Based on the objective circulation background of the Arctic region, the observations are defined as Area A and Area B (the red and blue scatter points in Figure 1, respectively). The reconstructed field and reanalysis field corresponding to the observation time are then interpolated to the observation locations, and the average values are calculated for analysis. The results are shown in Figure 10:

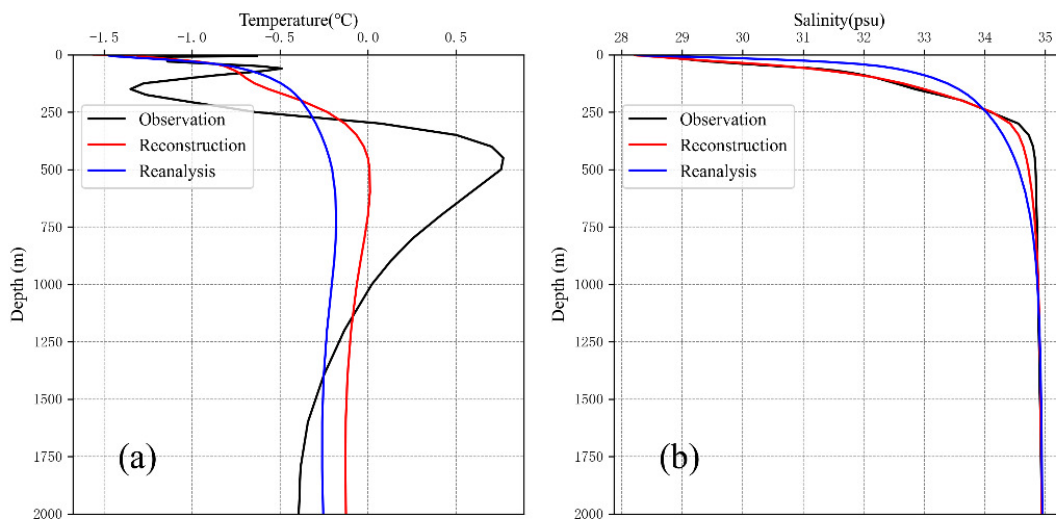


**Figure 10.** Cont.

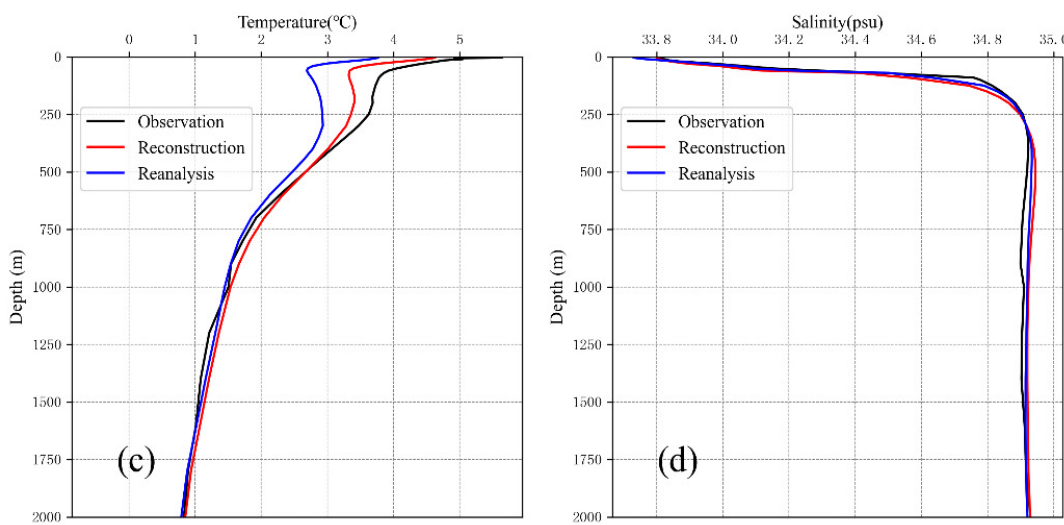


**Figure 10.** Average curves of field observations, reconstructed data, and reanalysis data. Where (a,b) show the average temperature and salinity values for Area B, respectively; and (c,d) show the same values for Area A. The black, red and blue lines, respectively, represent the observed values, reconstructed data, and reanalysis data.

The observed values in Area B show a distinct barrier layer around 150 m, which is not represented well in the reconstructed results. This is due to the same deficiency existing in the reanalysis data, and the statistical regression model could only be adjusted based on the reanalysis data used as a parameter library. For the salinity in Area B, the reconstructed data clearly match the observed results better than the reanalysis data, demonstrating the feasibility of inverting salinity in the Arctic region—especially in ice-covered areas—using SLA inversion. In Area A, the reconstructed data show good results for both temperature and salinity.

The seasonal variation of sea ice bears a significant impact on the three-dimensional thermohaline structure of the Arctic region. To assess the stability of reconstructed results at different times and locations, an Argo float (ID: 3901620) located in Area A and an ITP (ID: 110) located in Area B are selected for verification, as shown in Figure 1. The results are shown in Figures 11 and 12.

For the temperature time series, both the reconstructed results from the statistical regression model driven by satellite data and the ideal experiment results are found to capture the Argo in situ observations better than the reanalysis data. This is particularly evident in February 2019, where the reconstructed shallow layer temperatures are closed to the observations. These findings suggest that the satellite SST effectively improves the temperature reconstruction results in Area A. Regarding the salinity time series, while the overall trends are consistent, the ideal experiment results perform well. The satellite-reconstructed results, however, exhibit a considerable degree of noise, which is attributed to the influence of satellite SSS:

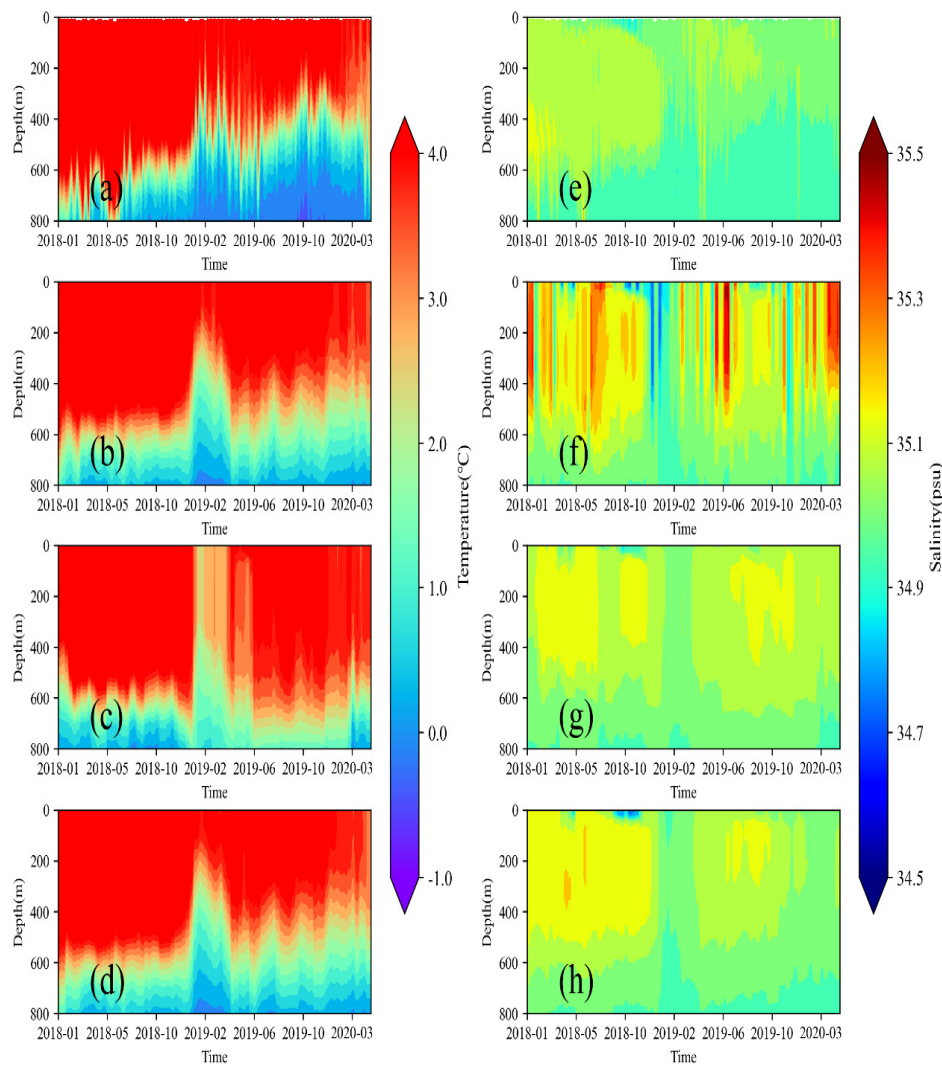


**Figure 11.** Time series of thermohaline structures from Argo data, satellite-driven reconstructed data, reanalysis data, and ideal experiment. Where (a–d), respectively, show the temperature time series from the Argo data, reconstructed data, reanalysis data, and ideal experiment; and (e–h) show the salinity time series from the same data sets.

In contrast to the characteristics observed in Area A, the reconstructed salinity in Area B was found to reflect the actual observed values better than the reanalysis salinity. This is attributed to the removal of the satellite-observed SSS term from the salinity relationship in ice-covered areas in the statistical regression method in this study. This indirectly indicates that sub-ice salinity changes are the primary cause of SLA variations [53,54], further confirming that the noise in the inverted salinity results for Area A is caused by satellite-observed SSS. Regarding the temperature time series, the reconstructed results driven by the satellite data, reanalysis results, and ideal experiments all exhibit consistent trends. However, all of these results deviate significantly from the observed values. This suggests that, while the statistical regression model constructed in this study adequately reflects the sub-ice temperature structure, there remains a considerable discrepancy with the in situ observation due to the complex dynamic processes in Area B.

Next, to investigate the differences in the three-dimensional thermohaline structure results based on sea ice seasonal variations under different data-driven experiments, a more detailed analysis of the driving data and inversion results is conducted. In ice-free areas, the consistency among the satellite data, reanalysis data, and in situ SST observations is reflected in the RMSE of the temperature reconstruction results, with the RMSE of reconstruction results driven by different data sources being nearly identical. The in situ

SSS in ice-free areas is quite consistent with the reanalysis SSS, while the satellite data SSS exhibits notable oscillations. This leads to the noise observed in the salinity time series in Figure 11f, and results in the RMSE of satellite-driven salinity reconstruction results for ice-free areas being greater in the shallow layer than that of the reanalysis data-driven ideal experiment. In ice-covered areas, the satellite-observed SST aligns well with the in situ ITP data, showing significant differences between the reanalysis SST. However, Figure 13g indicates no substantial difference in the RMSE of temperature reconstruction results is driven by satellite data and reanalysis data. Combined with the analysis from Figure 12, it is inferred that both the reanalysis and three-dimensional thermohaline reconstruction data exhibit certain errors in temperature structure compared to the observations. In addition, the accuracy of the salinity inversion results is potentially limited by the temporal resolution of satellite SLA products.

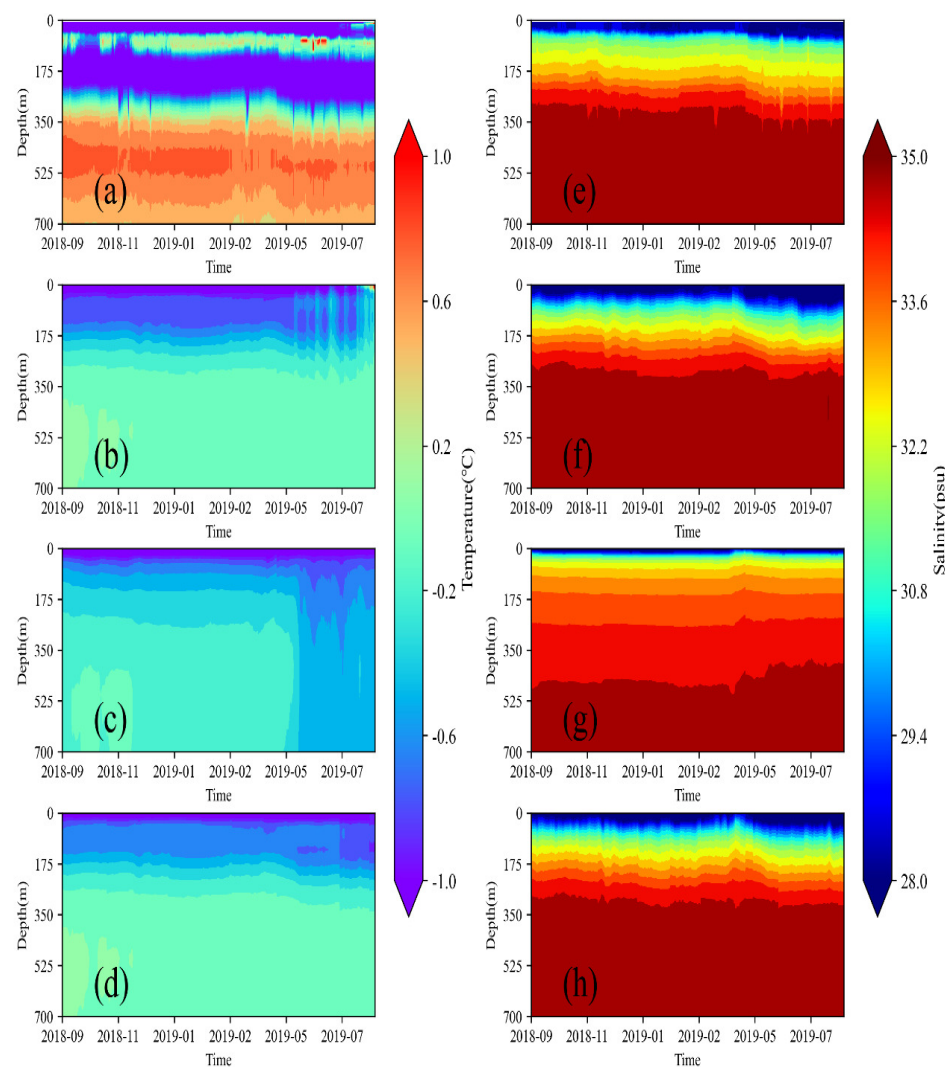


**Figure 12.** Time series of thermohaline structures from ITP data, satellite-driven reconstructed data, reanalysis data, and ideal experiment. Where (a–d), respectively, show the temperature time series from the ITP data, reconstructed data, reanalysis data, and ideal experiment; and (e–h) show the salinity time series from the same datasets.

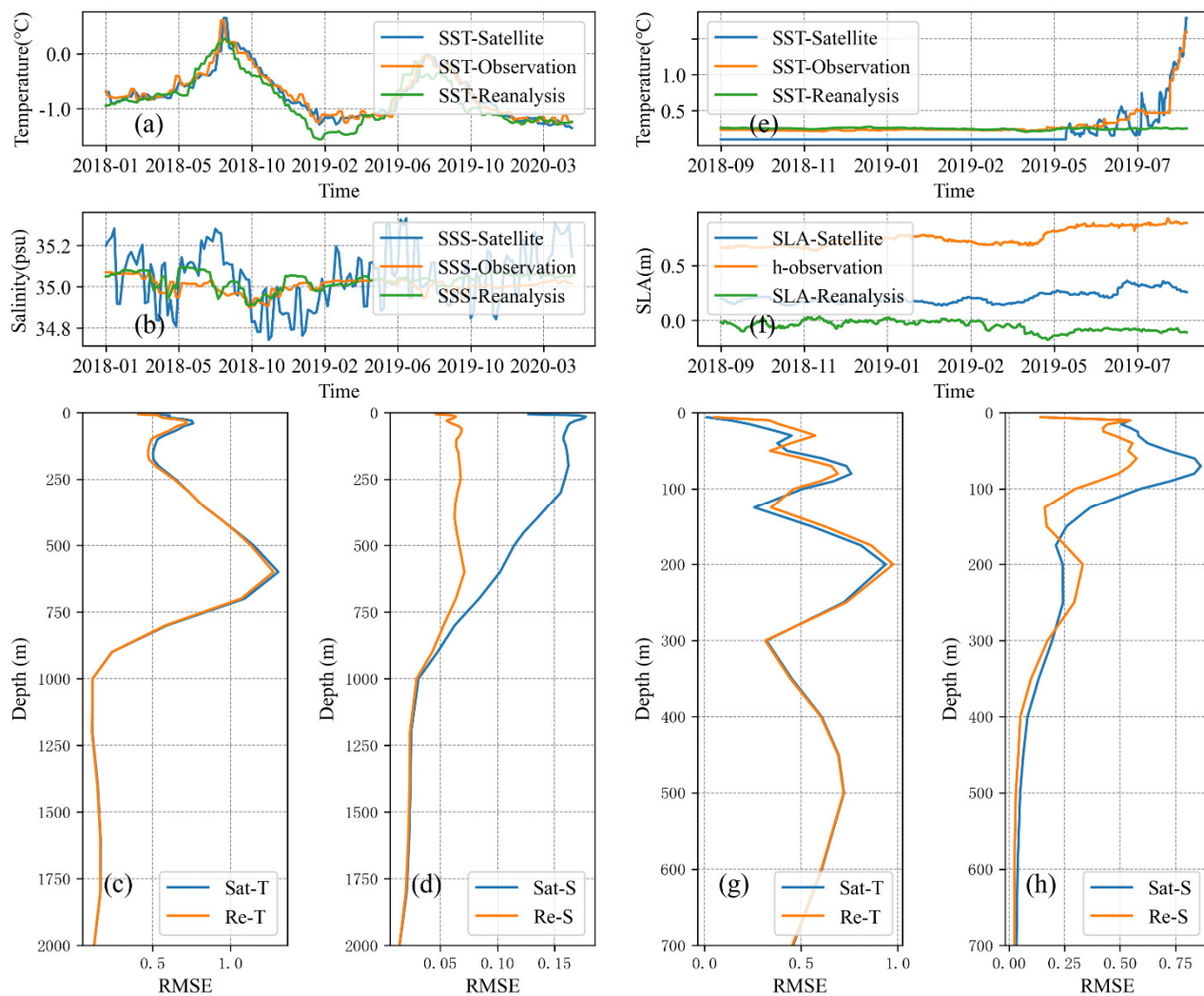


**Figure 13.** Where (a) shows the SST from satellite data, observational data (Argo 3901620), and reanalysis surface data for ice-free areas; (b) shows the same data for SSS; (c) shows the temperature RMSE of ideal experiment and satellite-driven inversion results compared to the Argo 3901620 data; (d) shows the same data for salinity; (e) presents the SST from the satellite data, observational data (ITP 110), and reanalysis surface data for ice-covered areas; (f) shows the same data for SLA; (g) illustrates the temperature RMSE of ideal experiment and satellite-driven inversion results compared to ITP 110 data; and (h) shows the same data for salinity.

Then, we compared the reconstructed field with in situ observations at the brown scatter points shown in Figure 1, and the results are shown in Figure 14. It can be seen that the temperature reconstruction field at the four single points is closer to in situ observations compared to the reanalysis field. Specifically, for the temperature structure under ice, there is an overall deviation between the reconstruction field and the reanalysis field in Figure 14e,f. For the salinity results, both point 1 and point 2 are in ice-free areas, but the salinity reconstruction effect at point 2 is greater than at point 1, which is due to the oscillation of satellite SSS. The shallow salinity reconstruction results at 2 points are consistent with the observed trend, while the reanalysis results at 0–100 m are contradictory to the observed trend. This indicates that using satellite SSS can effectively improve salinity reconstruction results when it matches the observations. For salinity in ice regions, the reconstructed results are superior to reanalysis data. From this, it can be observed that the method we used to reconstruct the thermohaline field is feasible.

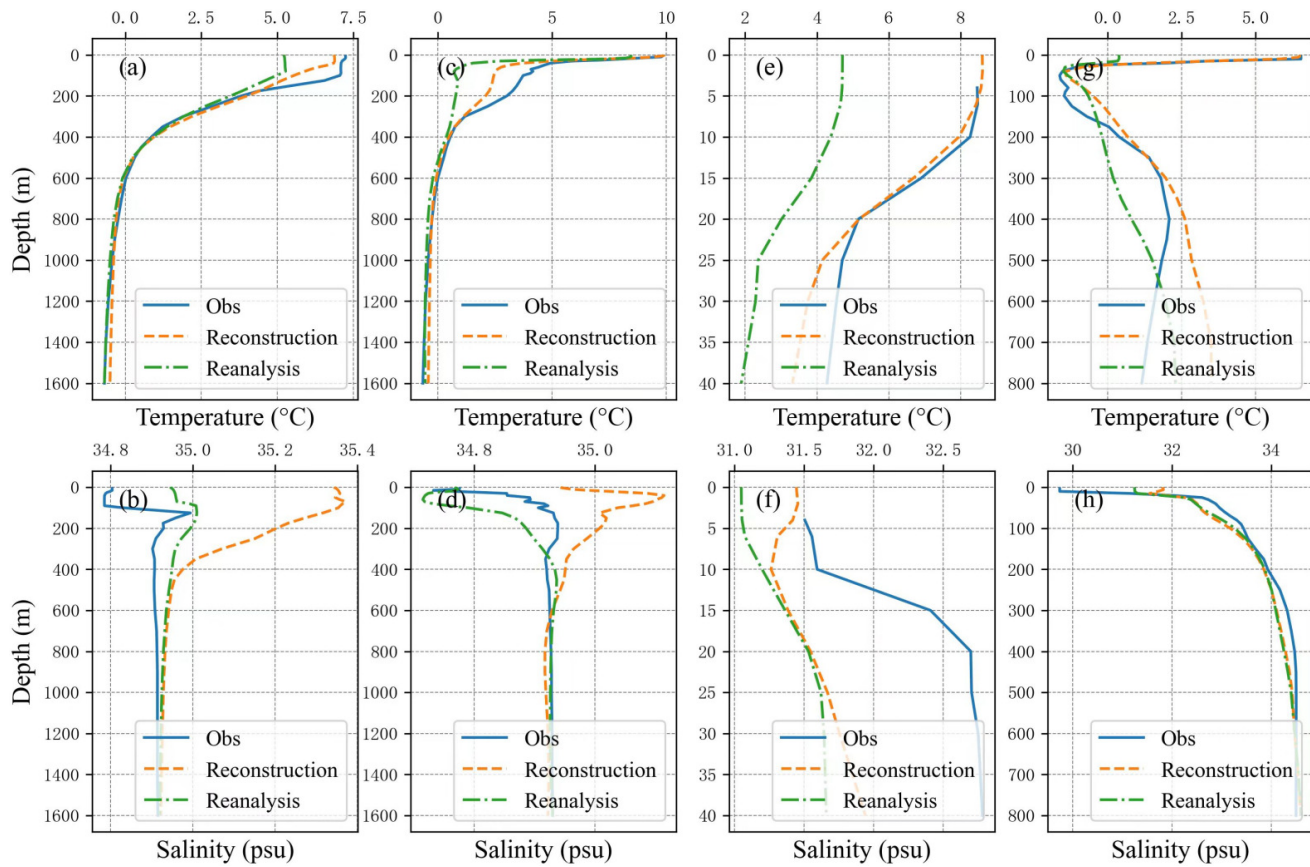


**Figure 14.** Where (a) shows the temperature from in situ observation, reconstruction, and reanalysis data at point 1; (b) shows the same data for salinity at point 1; (c,d) show those at point 2; (e,f) show those at point 3; (g,h) show those at point 4.

#### 4. Discussion

Considering the seasonal variations of Arctic sea ice, the study area is divided into ice-covered and ice-free regions, and a statistical regression model for the three-dimensional thermohaline structure based on satellite data is established. The reliability and stability of the three-dimensional thermohaline reconstruction results are validated through comparisons with TOPAZ reanalysis and in situ observational data. However, due to the complex dynamic processes in the Arctic sea area, there remains considerable room for improvement in the depiction of sub-ice thermohaline structures using the statistical regression model based on satellite remote sensing data.

#### 5. Conclusions and Future Work

In this study, we used statistical regression methods, combined with the concentration of sea ice in the Arctic Ocean, to invert the subsurface information of the ocean using satellite SST, SLA, and SSS data. On the basis of the TOPAZ reanalysis data used, this method projects the disturbance of sea surface information onto the subsurface to obtain a reconstructed three-dimensional thermohaline field, effectively utilizing the advantage of satellite observation's spatiotemporal continuity. However, it should be pointed out that due to the significant error in sea surface salinity observed by satellites in the Arctic compared to altitude observations, there may be abnormal oscillations in salinity reconstruction when inputting into satellite SSS, which can be improved with the development of satellite observation technology. However, for the temperature structure beneath the ice, reanalysis of the data did not simulate enough in situ observations, which might result in the poor performance of the temperature reconstruction field.

There is still room for improvement in using statistical regression models based on satellite remote sensing data to describe the thermohaline structure under ice. This is partly due to the significant difference in thermohaline structures between reanalysis data and in situ data under ice, and partly because there is still improvement required in the resolution and accuracy of satellite data. Next, we will use climatology based on in situ observations instead of reanalysis to depict a more realistic thermohaline structure beneath the ice. On the other hand, with the development of satellite remote sensing technology, especially sea ice remote sensing technology, emerging technologies represented by Global Navigation Satellite System-Reflectometry (GNSS-R) can provide more accurate satellite observation results [57,58]. This could reduce the error between reconstructed fields and in situ observations, improving our understanding of the three-dimensional thermohaline structure of the Arctic sea, and ultimately enhancing our ability to study and predict the impact of climate change in this critical region.

**Author Contributions:** Conceptualization, X.W. (Xiangyu Wu) and J.L.; methodology, X.W. (Xiangyu Wu) and J.L.; validation, X.W. (Xidong Wang); formal analysis, Z.H.; investigation, Z.C.; resources, S.R.; data curation, X.L.; writing—original draft preparation, X.W. (Xiangyu Wu) and J.L.; writing—review and editing, X.W. (Xiangyu Wu) and J.L. All authors have read and agreed to the published version of the manuscript.

**Funding:** This research was funded by National Key Research and Development Program of China, grant number 2023YFC3107703.

**Data Availability Statement:** The datasets presented in this article are not readily available because they are generated from proprietary equipment and are subject to commercial confidentiality.

**Conflicts of Interest:** The authors declare no conflicts of interest.

## References

1. Box, J.E. Key indicators of Arctic climate change: 1971–2017. *Environ. Res. Lett.* **2019**, *14*, 045010. [[CrossRef](#)]
2. Bekryaev, R.V.; Polyakov, I.V.; Alexeev, V.A. Role of polar amplification in long-term surface air temperature variations and modern Arctic warming. *J. Clim.* **2010**, *23*, 3888–3906. [[CrossRef](#)]
3. Cohen, J.; Screen, J.A.; Furtado, J.C.; Barlow, M.; Whittleston, D.; Coumou, D.; Francis, J.; Dethloff, K.; Entekhabi, D.; Overland, J.; et al. Recent Arctic amplification and extreme mid-latitude weather. *Nat. Geosci.* **2014**, *7*, 627–637. [[CrossRef](#)]
4. Serreze, M.C.; Barry, R.G. Processes and impacts of Arctic amplification: A research synthesis. *Glob. Planet. Chang.* **2011**, *77*, 85–96. [[CrossRef](#)]
5. Stroeve, J. Changing state of Arctic sea ice across all seasons. *Environ. Res. Lett.* **2018**, *13*, 103001. [[CrossRef](#)]
6. Meier, W.N.; Hovelsrud, G.K.; Van Oort, B.E.; Key, J.R.; Kovacs, K.M.; Michel, C.; Haas, C.; Granskog, M.A.; Gerland, S.; Perovich, D.K.; et al. Arctic sea ice in transformation: A review of recent observed changes and impacts on biology and human activity. *Rev. Geophys.* **2014**, *52*, 185–217. [[CrossRef](#)]
7. Sévellec, F.; Fedorov, A.V.; Liu, W. Arctic sea-ice decline weakens the Atlantic meridional overturning circulation. *Nat. Clim. Chang.* **2017**, *7*, 604–610. [[CrossRef](#)]
8. Lapeyre, G.; Klein, P. Dynamics of the upper oceanic layers in terms of surface quasigeostrophy theory. *J. Phys. Oceanogr.* **2006**, *36*, 165–176. [[CrossRef](#)]
9. Wang, J.; Flierl, G.R.; LaCasce, J.H.; McClean, J.L.; Mahadevan, A. Reconstructing the ocean’s interior from surface data. *J. Phys. Oceanogr.* **2013**, *43*, 1611–1626. [[CrossRef](#)]
10. Fox, D.N.; Barron, C.N.; Carnes, M.R.; Booda, M.; Peggion, G.; Van Gurley, J. The modular ocean data assimilation system. *Oceanography* **2002**, *15*, 22–28. [[CrossRef](#)]
11. Bub, F.L.; Mask, A.C.; Wood, K.R.; Krynen, D.G.; Lunde, B.N.; DeHaan, C.J.; Metzger, E.J.; Posey, P.G.; Wallmark, J.A. The Navy’s application of ocean forecasting to decision support. *Oceanography* **2014**, *27*, 126–137. [[CrossRef](#)]
12. He, Z.; Wu, X.; Jin, B.; Chen, Z.; Liu, J.; Wang, Z. Three-Dimensional Thermohaline Structure Reconstruction in the Northwest Pacific Ocean from HY-2 Satellite Data Based on a Variational Method. *J. Phys. Conf. Ser.* **2023**, *2486*, 012035. [[CrossRef](#)]
13. Han, M.; Feng, Y.; Zhao, X.; Sun, C.; Hong, F.; Liu, C. A Convolutional Neural Network Using Surface Data to Predict Subsurface Temperatures in the Pacific Ocean. *IEEE Access* **2019**, *7*, 172816–172829. [[CrossRef](#)]
14. Lou, R.; Lv, Z.; Dang, S.; Su, T. Application of Machine Learning in Ocean Data. *Multimed. Syst.* **2021**, *29*, 1815–1824. [[CrossRef](#)]
15. Carnes, M.R.; Mitchell, J.L.; de Witt, P.W. Synthetic temperature profiles derived from Geosat altimetry: Comparison with air-dropped expendable bathythermograph profiles. *J. Geophys. Res. Ocean.* **1990**, *95*, 17979–17992. [[CrossRef](#)]
16. Carnes, M.R.; Teague, W.J.; Mitchell, J.L. Inference of subsurface thermohaline structure from fields measurable by satellite. *J. Atmos. Ocean. Technol.* **1994**, *11*, 551–566. [[CrossRef](#)]

17. Nardelli, B.B.; Santoleri, R. Reconstructing synthetic profiles from surface data. *J. Atmos. Ocean. Technol.* **2004**, *21*, 693–703. [[CrossRef](#)]
18. Guinehut, S.; Le Traon, P.; Larnicol, G.; Philipps, S. Combining Argo and remote-sensing data to estimate the ocean three-dimensional temperature fields—A first approach based on simulated observations. *J. Mar. Syst.* **2004**, *46*, 85–98. [[CrossRef](#)]
19. Wang, X.; Han, G.; Li, W.; Qi, Y. The inversion of a three-dimensional temperature field using satellite-observed sea surface information (Chinese). *J. Trop. Oceanogr.* **2011**, *30*, 10–17.
20. Mao, Q.; Chu, X.; Yan, Y.; Qi, Y.; Wang, X.; Gong, J.; Cai, D.; Wu, Z.; Pan, C. Design and Implementation of a Three-Dimensional Dynamic Temperature and Salinity Field Reconstruction System for the South China Sea (Chinese). *J. Trop. Oceanogr.* **2013**, *32*, 1–8.
21. Tang, B. Reconstruction of ocean temperature and salinity profiles in the Northern South China Sea using satellite observations. *Front. Mar. Sci.* **2022**, *9*, 945835. [[CrossRef](#)]
22. Helber, R.W.; Townsend, T.L.; Barron, C.N.; Dastugue, J.M.; Carnes, M.R. *Validation Test Report for the Improved Synthetic Ocean Profile (ISOP) System, Part I: Synthetic Profile Methods and Algorithm*; Naval Research Laboratory Report NRL/MR/7320-13-9364; Naval Research Laboratory: Stennis Space Center, MS, USA, 2013.
23. He, Z.; Wang, X.; Wu, X.; Chen, Z.; Chen, J. Projecting three-dimensional ocean thermohaline structure in the North Indian Ocean from the satellite sea surface data based on a variational method. *J. Geophys. Res. Ocean.* **2021**, *126*, e2020JC016759. [[CrossRef](#)]
24. Hurlburt, H.E. Dynamic transfer of simulated altimeter data into subsurface information by a numerical ocean model. *J. Geophys. Res. Ocean.* **1986**, *91*, 2372–2400. [[CrossRef](#)]
25. Haines, K. A direct method for assimilating sea surface height data into ocean models with adjustments to the deep circulation. *J. Phys. Oceanogr.* **1991**, *21*, 843–868. [[CrossRef](#)]
26. Isern-Fontanet, J.; Lapeyre, G.; Klein, P.; Chapron, B.; Hecht, M.W. Three-dimensional reconstruction of oceanic mesoscale currents from surface information. *J. Geophys. Res. Ocean.* **2008**, *113*. [[CrossRef](#)]
27. Klein, P.; Isern-Fontanet, J.; Lapeyre, G.; Roullet, G.; Danioux, E.; Chapron, B.; Le Gentil, S.; Sasaki, H. Diagnosis of vertical velocities in the upper ocean from high resolution sea surface height. *Geophys. Res. Lett.* **2009**, *36*. [[CrossRef](#)]
28. González-Haro, C.; Isern-Fontanet, J. Global ocean current reconstruction from altimetric and microwave SST measurements. *J. Geophys. Res. Ocean.* **2014**, *119*, 3378–3391. [[CrossRef](#)]
29. Klein, P.; Hua, B.L.; Lapeyre, G.; Capet, X.; Le Gentil, S.; Sasaki, H. Upper ocean turbulence from high-resolution 3D simulations. *J. Phys. Oceanogr.* **2008**, *38*, 1748–1763. [[CrossRef](#)]
30. Lapeyre, G. What vertical mode does the altimeter reflect? On the decomposition in baroclinic modes and on a surface-trapped mode. *J. Phys. Oceanogr.* **2009**, *39*, 2857–2874. [[CrossRef](#)]
31. Chen, Z.; Wang, X.; Liu, L. Reconstruction of three-dimensional ocean structure from sea surface data: An application of isQG method in the Southwest Indian Ocean. *J. Geophys. Res. Ocean.* **2020**, *125*, e2020JC016351. [[CrossRef](#)]
32. Liu, L.; Peng, S.; Wang, J.; Huang, R.X. Retrieving density and velocity fields of the ocean's interior from surface data. *J. Geophys. Res. Ocean.* **2014**, *119*, 8512–8529. [[CrossRef](#)]
33. Su, H.; Wang, A.; Zhang, T.; Qin, T.; Du, X.; Yan, X.-H. Super-resolution of subsurface temperature field from remote sensing observations based on machine learning. *Int. J. Appl. Earth Obs. Geoinf.* **2021**, *102*, 102440. [[CrossRef](#)]
34. Meng, Y.; Rigall, E.; Chen, X.; Gao, F.; Dong, J.; Chen, S. Physics-guided generative adversarial networks for sea subsurface temperature prediction. *IEEE Trans. Neural Netw. Learn. Syst.* **2021**, *34*, 3357–3370. [[CrossRef](#)] [[PubMed](#)]
35. Yang, J.; Mu, J.; Gu, H.; Xun, J. Research progress on intelligent detection of three-dimensional ocean temperature and salinity fields based on remote sensing(Chinese). *Digit. Ocean. Warf.* **2024**, *7*, 9–19.
36. Stark, J.D.; Donlon, C.J.; Martin, M.J.; McCulloch, M.E. OSTIA: An operational, high resolution, real time, global sea surface temperature analysis system. In Proceedings of the Oceans 2007-Europe, Aberdeen, UK, 18–21 June 2007; pp. 1–4.
37. Donlon, C.J.; Martin, M.; Stark, J.; Roberts-Jones, J.; Fiedler, E.; Wimmer, W. The operational sea surface temperature and sea ice analysis (OSTIA) system. *Remote Sens. Environ.* **2012**, *116*, 140–158. [[CrossRef](#)]
38. Good, S.; Fiedler, E.; Mao, C.; Martin, M.J.; Maycock, A.; Reid, R.; Roberts-Jones, J.; Searle, T.; Waters, J.; While, J.; et al. The Current Configuration of the OSTIA System for Operational Production of Foundation Sea Surface Temperature and Ice Concentration Analyses. *Remote Sens.* **2020**, *12*, 720. [[CrossRef](#)]
39. Prandi, P.; Poisson, J.-C.; Faugère, Y.; Guillot, A.; Dibarboire, G. Arctic sea surface height maps from multi-altimeter combination. *Earth Syst. Sci. Data Discuss.* **2021**, *2021*, 1–29. [[CrossRef](#)]
40. Martínez, J.; Gabarró, C.; Turiel, A.; González-Gambau, V.; Umbert, M.; Hoareau, N.; González-Haro, C.; Olmedo, E.; Arias, M.; Catany, R.; et al. Improved BEC SMOS Arctic Sea Surface Salinity product v3. *Earth Syst. Sci. Data* **2022**, *14*, 307–323. [[CrossRef](#)]
41. Sakov, P.; Counillon, F.; Bertino, L.; Lisæter, K.A.; Oke, P.R.; Koralev, A. TOPAZ4: An ocean-sea ice data assimilation system for the North Atlantic and Arctic. *Ocean Sci.* **2012**, *8*, 633–656. [[CrossRef](#)]
42. Hackett, B.; Burud, A.; Wakamatsu, T.; Melsom, A. ARCTIC\_ANALYSISFORECAST\_PHY\_002\_001 ARCTIC\_ANALYSISFORECAST\_BGC\_002\_004 ARCTIC\_ANALYSISFORECAST\_PHY\_ICE\_002\_011 ARCTIC\_ANALYSISFORECAST\_PHY\_TIDE\_002\_015 ARCTIC\_MULTIYEAR\_PHY\_002\_003 ARCTIC\_MULTIYEAR\_BGC\_002\_005. Available online: <https://catalogue.marine.copernicus.eu/documents/PUM/CMEMS-ARC-PUM-002-ALL.pdf> (accessed on 10 September 2024).
43. Bertino, L.; Lisæter, K.A. The TOPAZ monitoring and prediction system for the Atlantic and Arctic Oceans. *J. Oper. Oceanogr.* **2008**, *1*, 15–18. [[CrossRef](#)]

44. Koblinsky, C.; Smith, N.; Eds Argo Science Team. The global array of profiling floats. In *Observing Oceans in the 21st Century*; GODAE Project; Bureau of Meteorology: Melbourne, Australia, 2001; pp. 248–258.
45. Krishfield, R.; Toole, J. *ITP Data Processing Procedures*; Woods Hole Oceanographic Institution: Woods Hole, MA, USA, 2008.
46. Steele, M.; Morley, R.; Ermold, W. PHC: A Global Ocean Hydrography with a High-Quality Arctic Ocean. *J. Clim.* **2001**, *14*, 2079–2087. [CrossRef]
47. Fetterer, F.; Knowles, K.; Meier, W.; Savoie, M.; Windnagel, A. Sea Ice Index 2002. Available online: <https://nsidc.org/sites/nsidc.org/files/technical-references/Interpretation-Resources-for-Sea-Ice-Trends-and-Anomalies.pdf> (accessed on 10 September 2024).
48. Comiso, J.C.; Cavalieri, D.J.; Markus, T. Sea ice concentration, ice temperature, and snow depth using AMSR-E data. *IEEE Trans. Geosci. Remote Sens.* **2003**, *41*, 243–252. [CrossRef]
49. Polyak, L.; Alley, R.B.; Andrews, J.T.; Brigham-Grette, J.; Cronin, T.M.; Darby, D.A.; Dyke, A.S.; Fitzpatrick, J.J.; Funder, S.; Holland, M.; et al. History of sea ice in the Arctic. *Quat. Sci. Rev.* **2010**, *29*, 1757–1778. [CrossRef]
50. Swan, A.M.; Long, D.G. Multiyear Arctic sea ice classification using QuikSCAT. *IEEE Trans. Geosci. Remote Sens.* **2012**, *50*, 3317–3326. [CrossRef]
51. Goessling, H.F.; Tietsche, S.; Day, J.J.; Hawkins, E.; Jung, T. Predictability of the Arctic sea ice edge. *Geophys. Res. Lett.* **2016**, *43*, 1642–1650. [CrossRef]
52. Liang, X.; Losch, M.; Nerger, L.; Mu, L.; Yang, Q.; Liu, C. Using sea surface temperature observations to constrain upper ocean properties in an Arctic sea ice-ocean data assimilation system. *J. Geophys. Res. Ocean.* **2019**, *124*, 4727–4743. [CrossRef]
53. Benveniste, J.; Cazenave, A.; Champollion, N. *Integrative Study of the Mean Sea Level and Its Components*, 1st ed.; Space Sciences Series of ISSI; Springer International Publishing: Cham, Switzerland, 2017; ISBN 978-3-319-56490-6.
54. Raj, R.P.; Andersen, O.B.; Johannessen, J.A.; Gutknecht, B.D.; Chatterjee, S.; Rose, S.K.; Bonaduce, A.; Horwath, M.; Rannadal, H.; Richter, K.; et al. Arctic Sea Level Budget Assessment during the GRACE/Argo Time Period. *Remote Sens.* **2020**, *12*, 2837. [CrossRef]
55. He, Z.; Wang, X.; Chen, Z.; Fan, K. Study on the Method of Inverting Salinity Profiles Using Ocean Temperature Profiles and Sea Surface Salinity (Chinese). *J. Trop. Oceanogr.* **2021**, *40*, 41–51.
56. Chen, Z.; Wang, X.; Wu, X.; Cao, Y.; He, Z.; Wang, D.; Chen, J. Three-dimensional thermohaline structure estimation derived from HY-2 satellite data over the Maritime Silk Road and its applications. *Acta Oceanol. Sin.* **2024**, *43*, 41–53. [CrossRef]
57. Xie, Y.; Yan, Q. Retrieval of sea ice thickness using FY-3E/GNOS-II data. *Satell. Navig.* **2024**, *5*, 17. [CrossRef]
58. Xie, Y.; Yan, Q. Stand-alone retrieval of sea ice thickness from FY-3E GNOS-R data. *IEEE Geosci. Remote Sens. Lett.* **2024**, *21*, 2000305. [CrossRef]

**Disclaimer/Publisher’s Note:** The statements, opinions and data contained in all publications are solely those of the individual author(s) and contributor(s) and not of MDPI and/or the editor(s). MDPI and/or the editor(s) disclaim responsibility for any injury to people or property resulting from any ideas, methods, instructions or products referred to in the content.